

Probabilistic Occupancy Grid for Radio-Based SLAM

Xuhong Li*, Erik Leitinger[†], Fredrik Tufvesson*, and Florian Meyer[‡]

*Department of Electrical and Information Technology, Lund University, Sweden.

[†]Institute of Comm. Networks and Satellite Comms., Graz University of Technology, Austria

[‡]Department of Electrical and Computer Engineering, University of California San Diego, USA

Email: {xuhong.li, fredrik.tufvesson}@eit.lth.se, erik.leitinger@tugraz.at, flmeyer@ucsd.edu

Abstract—Sensing is an integral part of 6G and beyond systems, providing exceptional environmental perception along with communication. Radio frequency (RF)–based sensing often relies on simplified geometric assumptions (e.g., point scatterers or planar surfaces) to model specular multipath and keep inference tractable. However, such representations are not physically informative and fail to accurately capture extended objects with complex shapes and properties. This paper presents a probabilistic occupancy grid framework for radio-based simultaneous localization and mapping (SLAM), jointly reconstructing geometric structures and their radio-related properties. The proposed occupancy grid map representation is integrated into a multipath-based SLAM (MP-SLAM) formulation to enable simultaneous mobile-agent localization and environment mapping using multipath measurements.

To connect RF measurements with the grid map, a surface model is employed to describe candidate reflection paths, while occupancy grid cell states capture measurement uncertainties and fine-grained geometric details. Object RF-related properties are modeled via reflection coefficients. The proposed framework offers a principled, proof-of-concept approach to physically interpretable radio-based mapping, and simulation results demonstrate accurate reconstruction of geometry and material properties, as well as high-accuracy localization. In addition, the results highlight the potential to use prior occupancy maps obtained from other radio devices or complementary sensors for subsequent map extension and refinement.

I. INTRODUCTION

Location and environment awareness are integrated capabilities of future 6G communication networks, supporting applications such as location-aware security, autonomous systems, and digital twins in diverse scenarios, notably indoor and urban environments. In such environments, dense available infrastructure facilitates radio-based sensing [1]. However, the impact of complex geometries with heterogeneous electromagnetic properties on RF signal propagation cannot be sufficiently captured with simple parametric geometric models (e.g., virtual anchors (VAs), scatterers or smooth surfaces) commonly used in existing mapping methods [2]–[5], motivating the need for more realistic and physically informed environment mapping methods.

For perception of complex environment, a well established approach is occupancy grid mapping, which discretizes the environment into fine spatial cells, each associated to a random variable encoding the probability of occupancy. This representation also facilitates multi-sensor fusion by providing a shared spatial frame that supports consistent map updates over

This work was supported in part by the Knut and Alice Wallenberg Foundation under WASP Scholarship Program (KAW 2023.0509), in part by the Austrian Research Promotion Agency (FFG) under the PRISM project (620753), and in part by the European Union’s Horizon Europe research and innovation program under Grant 101192113.

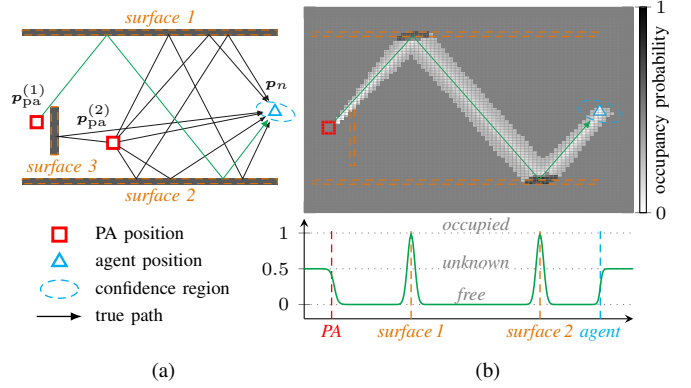


Fig. 1: (a) Geometrical depiction of a distributed multiple-input-multiple-output (MIMO) radio propagation environment consisting of three reflective surfaces, two physical anchors (PAs) and a mobile agent. (b) Illustration of the interaction between grid cells and the radio frequency (RF) double-bounce path (cyan) from PA 1 at position $p_{pa}^{(1)}$ to the mobile agent at p_n , accounting for measurement and agent position uncertainties. The resulting occupancy probability profile is also shown, where transversal cells converge toward *free* occupancy, surface-hit cells toward *occupied*, and all other cells remain in an *unknown* (unexplored) state.

time. Grid mapping is widely used in robotics for applications like navigation and simultaneous localization and mapping (SLAM) [6]–[11], where direct or single-bounce ray and independence between grid cell states are commonly assumed to maintain inference tractability. However, its application to radio-based mapping [12] remains limited given substantial computational and modeling challenges. Geometrically, it is difficult to identify how RF signals interact with grid cells, especially in strong multipath propagation scenarios where higher-order bounce paths can contribute substantially to the received RF signals and convey rich structural information [13], [14]. Besides, it is necessary to consider the statistical dependence between occupancy states of grid cells, when they are traversed or hit by the same propagation path or jointly influenced by multiple interacting paths from one or more devices. In addition, jointly inferring grid occupancy states and mobile agent state within a unified Bayesian framework that encodes time-varying radio channel information and uncertainties is highly complex.

Feature-based multipath-based SLAM (MP-SLAM) methods [2]–[5], [15] provide the principled foundation for the integration of the occupancy-grid. MP-SLAM exploiting VAs or surfaces models is proven reliable in modeling and estimating dominant RF propagation paths such as line-of-sights (LoSs) and specular reflections. In particular, [16], [17] has demonstrated reliable ray tracing with up to double-

bounce paths using adaptive data fusion. These feature models can be integrated into a hierarchical geometric representation within MP-SLAM to explain possible RF signal–environment interaction processes, while occupancy-grid cell states capture fine map details. In addition, the MP-SLAM problem can be efficiently formulated as a factorized posterior on a factor graph representation [15], [16], and approximate inference is performed applying the message passing rules of sum-product algorithm (SPA) [18], [19]. This structure yields highly scalable algorithms and naturally accommodates extensions like occupancy grid and support adaptive data fusion.

Contribution: In this work, we introduce a Bayesian MP-SLAM algorithm that jointly localizes the mobile agent and estimates the occupancy states of grid cells, allowing the mapping of complex environmental geometries using distributed multiple-input-multiple-output (D-MIMO) systems [20]–[23]. Based on our previous work of MP-SLAM [16], [17], we established a hierarchical geometric model that involves (i) surface feature vectors (SFVs) modeling reflective surfaces and associated signal attenuation factors and (ii) occupancy grid cells. With SFVs, we resolve candidate reflected paths up to double bounces. The Bayesian estimation of the agent state, SFV states, and cell occupancy states is established by applying the message passing algorithm to the factor graph representation of the proposed statistical model. We exploit a forward sensor model considering the statistical dependence between grid cells and to jointly update their occupancy states after fusing information across detected propagation paths and base stations (BSs). Measurement variances that capture uncertainties in range, angle, amplitude, and related parameters are characterized through amplitude statistics through Fisher information, thereby refining the measurement likelihoods and enabling rich channel information to be encoded into grid states. Using synthetic data, this proof-of-concept study demonstrates (i) accurate localization and mapping performance and (ii) the ability to continuously expand and update an established map.

II. GEOMETRICAL RELATIONS

We consider a D-MIMO system operating in a two-dimensional (2D) dynamic scenario with horizontal-only signal propagation. At each discrete time n , J distributed static PAs (e.g., BSs) at known positions $\mathbf{p}_{\text{pa}}^{(j)} = [p_{\text{pa},x}^{(j)} \ p_{\text{pa},y}^{(j)}]^T \in \mathbb{R}^{2 \times 1}$ and $j \in \{1, \dots, J\}$ transmit RF signals, which are received by the mobile agent at unknown and time-varying position $\mathbf{p}_n = [p_{n,x} \ p_{n,y}]^T \in \mathbb{R}^{2 \times 1}$. Each PA is equipped with a H_{tx} -element antenna array with known orientation $\Delta\phi^{(j)}$, and the mobile agent is equipped with a H_{rx} -element antenna array with unknown orientation $\Delta\varphi_n$.

In the RF propagation environment (i.e., region-of-interest (RoI)), there exist S static reflective surfaces, which are indexed by $s \in \mathcal{S} \triangleq \{1, \dots, S\}$ and modeled by SFVs at positions $\mathbf{p}_{s,\text{sfv}} \in \mathbb{R}^{2 \times 1}$ denoting the mirror images of the origin $[0, 0]^T$ on the surfaces. We consider specular multipath components with up to two reflections. Each of the reflected paths can be modeled by a VA at position $\mathbf{p}_{ss',\text{va}}^{(j)} \in \mathbb{R}^{2 \times 1}$ that denotes the mirror image of the j th PA on these surfaces, where the index tuple $(s, s') \in \mathcal{D} \triangleq \{(s, s') \in \mathcal{S} \times \mathcal{S}\}$ denotes the signal interaction order from the s' th surface

to the s th surface before reaching the mobile agent. The two sets $\mathcal{D}_S \triangleq \{(s, s) \in \mathcal{S} \times \mathcal{S}\}$ with $|\mathcal{D}_S| = S$ and $\mathcal{D}_D \triangleq \{(s, s') \in \mathcal{S} \times \mathcal{S} | s \neq s'\}$ with $|\mathcal{D}_D| = S(S-1)$ contain the index tuples for single-bounce and double-bounce VAs, respectively. Therefore, the maximum number of VAs for PA j is given by $|\mathcal{D}| = S + S(S-1)$ and $\mathcal{D} = \mathcal{D}_S \cup \mathcal{D}_D$. For each propagation path, its distance $d_{ss',n}^{(j)}$, angle-of-departure (AoD) $\phi_{ss',n}^{(j)}$ and angle-of-arrival (AoA) $\varphi_{ss',n}^{(j)}$ are modeled by $d_{ss',n}^{(j)} = \|\mathbf{p}_n - \mathbf{p}_{ss',\text{va}}^{(j)}\|$, $\phi_{ss',n}^{(j)} = \angle(\mathbf{p}_{\text{IP}_{ss',n}}^{(j)}, \mathbf{p}_{\text{pa}}, \Delta\phi^{(j)})$ and $\varphi_{ss',n}^{(j)} = \angle(\mathbf{p}_n, \mathbf{p}_{ss',\text{va}}^{(j)}, \Delta\varphi_n)$, and $\mathbf{p}_{\text{IP}_{ss',n}}^{(j)}$ denotes the interaction point (IP) of the path on the first interacting surface s' . The geometric transformation between $\mathbf{p}_{ss',\text{va}}^{(j)}$, $\mathbf{p}_{s',\text{va}}^{(j)}$ and $\mathbf{p}_{\text{IP}_{ss',n}}^{(j)}$ and $\mathbf{p}_{s,\text{sfv}}$, $\mathbf{p}_{s',\text{sfv}}$ and \mathbf{p}_{pa} is provided in [16, Section II A].

The RoI is assumed to be partitioned into continuously located grid cells with index $i \in \mathcal{Q} \triangleq \{1, \dots, Q\}$, and Q is number of all cells. As shown in Fig. 1, each propagation path interacts with a subset of cells $\mathcal{Q}_{ss',n}^{(j)}$, i.e., the traversed cells $\tilde{\mathcal{Q}}_{ss',n}^{(j)}$ providing evidence of free space and the hit cells $\tilde{\tilde{\mathcal{Q}}}_{ss',n}^{(j)}$ which denote path–object interactions and provide occupancy evidence. The remaining cells are denoted as $\tilde{\mathcal{Q}}_{ss',n}^{(j)} = \mathcal{Q} \setminus \{\mathcal{Q}_{ss',n}^{(j)} \cup \tilde{\tilde{\mathcal{Q}}}_{ss',n}^{(j)}\}$. The sets of cells are identified by performing ray casting [6], [9].

III. SYSTEM MODEL

At each time n , the state of the mobile agent is given by $\mathbf{x}_n \triangleq [\beta_n^T \ \Delta\varphi_n]^T$ with $\beta_n^T \triangleq [\mathbf{p}_n^T \ \mathbf{v}_n^T]^T$. The state vector consists of the position \mathbf{p}_n , the velocity $\mathbf{v}_n = [v_{x,n} \ v_{y,n}]^T$ and the orientation of the azimuth array $\Delta\varphi_n$. The stacked agent state vector for all time steps up to n is given by $\mathbf{x}_{1:n} \triangleq [\mathbf{x}_1^T \ \dots \ \mathbf{x}_n^T]^T$. Following [16], we account for the unknown and time-varying number of SFVs at each time step n by introducing potential SFVs (PSFVs) indexed by $s \in \{1, \dots, S_n\}$, where S_n represents the maximum possible number of PSFVs that produced at least one measurement so far. PSFV states are modeled as $\mathbf{y}_{s,n} \triangleq [\mathbf{p}_{s,\text{sfv}}^T \ \rho_s \ r_{s,n}]^T$ where $\mathbf{p}_{s,\text{sfv}}$ and ρ_s denote the position and reflection coefficient for each ray interaction. The existence or non-existence of the s th PSFV is modeled by a binary random variable $r_{s,n} \in \{1, 0\}$, and it exists if and only if $r_{s,n} = 1$.

The PSFVs that have been detected either at a previous time $n' < n$, or at time n but at a previous PA $j' < j$ are referred to as *legacy PSFVs* with states $\underline{\mathbf{y}}_{s,n}^{(j)} \triangleq [\mathbf{p}_{s,\text{sfv}}^{(j)T} \ \rho_s^{(j)} \ r_{s,n}^{(j)}]^T$. The stacked PSFV state vector is given by $\underline{\mathbf{y}}_n^{(1)} \triangleq [\underline{\mathbf{y}}_{1,n}^{(1)T} \ \dots \ \underline{\mathbf{y}}_{S_{n-1},n}^{(1)T}]^T$ at PA $j = 1$, or $\underline{\mathbf{y}}_n^{(j)} \triangleq [\underline{\mathbf{y}}_{1,n}^{(j)T} \ \dots \ \underline{\mathbf{y}}_{S_n^{(j-1)},n}^{(j)T}]^T$ at PA $j > 1$. *New SFVs* that generate measurements for the first time are modeled by a Poisson point process with mean μ_n and conditional probability density function (PDF) $f_n(\bar{\mathbf{p}}_{m,\text{sfv}}^{(j)}, \bar{\rho}_m^{(j)} | \mathbf{x}_n)$. The state of new PSFVs is given by $\bar{\mathbf{y}}_{m,n}^{(j)} \triangleq [\bar{\mathbf{p}}_{m,\text{sfv}}^{(j)T} \ \bar{\rho}_m^{(j)} \ \bar{r}_{m,n}^{(j)}]^T$, $m \in \{1, \dots, M_n^{(j)}\}$. The state vector of all new PSFVs at PA j is given by $\bar{\mathbf{y}}_n^{(j)} \triangleq [\bar{\mathbf{y}}_{1,n}^{(j)T} \ \dots \ \bar{\mathbf{y}}_{M_n^{(j)},n}^{(j)T}]^T$. New PSFVs become legacy PSFVs after the next measurements either of the next PA or at the next time they are observed. The number of legacy PSFVs is updated according to $S_n^{(1)} = S_{n-1}^{(j)} + M_n^{(1)}$ for $j = 1$, and

$S_n^{(j)} = S_n^{(j-1)} + M_n^{(j)}$ for $j > 1$. After the measurements of all J PAs have been incorporated at time n , the state of all PSFV states at time n is given by $\mathbf{y}_n \triangleq [\mathbf{y}_n^{(J)T} \bar{\mathbf{y}}_n^{(J)T}]^T$, which is further stacked into the vector for all times up to n given by $\mathbf{y}_{1:n} \triangleq [\mathbf{y}_1^T \cdots \mathbf{y}_n^T]^T$. To account for the time-varying LoS condition from PA j to the agent, we define the PA state as $\underline{\mathbf{y}}_{0,n}^{(j)} \triangleq [\underline{\mathbf{p}}_{0,\text{sfv}}^{(j)T} \underline{\rho}_0^{(j)} \underline{\mathbf{r}}_{0,n}^{(j)}]^T$, with $\underline{\mathbf{p}}_{0,\text{sfv}}^{(j)} \triangleq \mathbf{p}_{\text{pa}}^{(j)}$ and $\underline{\rho}_0^{(j)} \triangleq 1$. The set $\tilde{\mathcal{D}}_n^{(j)} \triangleq (0, 0) \cup \mathcal{D}_n^{(j)}$ represents all propagation paths at PA j and time n including the LoS.

A. Grid Cell State

The occupancy state of each cell is modeled as a binary random variable $o_{i,n} \in \{0, 1\}$ with $i \in \{1, \dots, Q\}$, where $o_{i,n} = 0$ indicates a free cell, $o_{i,n} = 1$ indicates an occupied cell. The corresponding probabilities are given by $p(o_{i,n} = 0)$ and $p(o_{i,n} = 1) = 1 - p(o_{i,n} = 0)$, respectively. The stacked vector of all cell states is given by $\mathbf{o}_n \triangleq [o_{1,n} \cdots o_{Q,n}]^T$ at time n , and $\mathbf{o}_{0:n} \triangleq [\mathbf{o}_0^T \cdots \mathbf{o}_n^T]^T$ at all times up to n . Note that the grid cell states are physically time-invariant in stationary environment. The time dependence serves only to model the inference process. We further define the following set representing the valid spatial prerequisite for an existing path (s, s') : $\mathcal{V}_{ss',n}^{(j)} \triangleq \left\{ \mathbf{o}_n : o_{i,n} = 0 \ \forall i \in \tilde{\mathcal{Q}}_{ss',n}^{(j)}, o_{i',n} = 1 \ \forall i' \in \tilde{\mathcal{Q}}_{ss',n}^{(j)} \right\}$. The corresponding joint probability mass function (PMF) $p_{\mathcal{V}_{ss',n}^{(j)}} \triangleq p(\mathbf{o}_n | \mathbf{o}_n \in \mathcal{V}_{ss',n}^{(j)})$ is determined as

$$p(\mathbf{o}_n | \mathbf{o}_n \in \mathcal{V}_{ss',n}^{(j)}) \quad (1)$$

$$= \left(\prod_{i \in \tilde{\mathcal{Q}}_{ss',n}^{(j)}} p(o_{i,n} = 0) \right) \left(1 - \prod_{i' \in \tilde{\mathcal{Q}}_{ss',n}^{(j)}} (1 - p(o_{i',n} = 1)) \right).$$

For the set traversed $\tilde{\mathcal{Q}}_{ss',n}^{(j)}$, high-occupancy cells along the path are penalized, as they indicate potential obstacles that attenuate the likelihood of the path. Similarly for the hit set $\tilde{\mathcal{Q}}_{ss',n}^{(j)}$, high-occupancy hit cells further decrease the probability of a blocked path. This model improves sensitivity to the prior information encoded in the occupancy map.

B. Measurement Model

The mobile agent state and PSFV states relate to the distance measurements $z_{dm,n}^{(j)}$, the AoD measurements $z_{\phi m,n}^{(j)}$, the AoA measurements $z_{\varphi m,n}^{(j)}$, and the normalized amplitude measurements $z_{um,n}^{(j)} \in [u_{\text{de}}, \infty)$ via likelihood functions (LHFs), which are assumed to be conditionally independent across m . Note that the measurements are obtained by applying a parametric channel estimation algorithm to RF measurements [24]–[26] in the pre-processing stage, where a detection threshold u_{de} is used. The LHFs for the LoS paths $f_P(z_{m,n}^{(j)} | \mathbf{p}_n, u_{00,n}^{(j)})$, for the single-bounce paths $f_S(z_{m,n}^{(j)} | \mathbf{p}_n, \mathbf{p}_{s,\text{sfv}}^{(j)}, u_{ss,n}^{(j)})$, for the double bounce paths $f_D(z_{m,n}^{(j)} | \mathbf{p}_n, \mathbf{p}_{s,\text{sfv}}^{(j)}, \mathbf{p}_{s',\text{sfv}}^{(j)}, u_{ss',n}^{(j)})$ and for the new paths $f_N(z_{m,n}^{(j)} | \mathbf{p}_n, \bar{\mathbf{p}}_{m,\text{sfv}}^{(j)}, \bar{u}_{m,n}^{(j)})$, as well as the individual LHFs of the distance $f_{ss'}^{(j)}(z_{dm,n}^{(j)})$, AoD $f_{\phi m}^{(j)}(z_{\phi m,n}^{(j)})$, AoA $f_{\varphi m}^{(j)}(z_{\varphi m,n}^{(j)})$ and the norm amplitude $f_{ss'}^{(j)}(z_{um,n}^{(j)})$ are in line with those presented in [17].

The normalized amplitude $u_{ss',n}^{(j)}$ is defined as the square root of the propagation path's signal-to-noise ratio (SNR). Assume that the path amplitude follows free-space pathloss and is attenuated by the reflection coefficient $\underline{\rho}_s$ after each surface reflection, $u_{ss',n}^{(j)}$ is given by

$$u_{ss',n}^{(j)} = \beta_{ss',n}^{(j)} \sqrt{H_{\text{rx}} P_{\text{tx}} \lambda_c / (4\pi d_{ss',n}^{(j)} \sigma_n)} \quad (2)$$

where λ_c is the wavelength at center frequency, P_{tx} is the known total transmit power, σ_n is the noise standard deviation (STD) provided by the parametric channel estimator, and $\beta_{ss',n}^{(j)}$ is the amplitude attenuation factor given as $\beta_{ss',n}^{(j)} = \underline{\rho}_s \underline{\rho}_{s'}$, and $\beta_{ss,n}^{(j)} = \underline{\rho}_s$. The normalized amplitude for new paths $\bar{u}_{m,n}$ is also obtained as in (2) with $\beta_{m,n}^{(j)} = \bar{\rho}_m$. The normalized amplitude is directly related to the detection probability $p_{d,ss'}^{(j)} = p_d(u_{ss',n}^{(j)})$ with $(s, s') \in \tilde{\mathcal{D}}_n^{(j)}$ and measurement variances via Fisher information [17].

C. State Evolution

The agent state, legacy PSFV states and cell states are assumed to evolve independently across j and n according to state-transition PDFs $f(\mathbf{x}_n | \mathbf{x}_{n-1})$, $f(\underline{\mathbf{y}}_{s,n} | \underline{\mathbf{y}}_{s,n-1})$ and $f(o_{i,n} | o_{i,n-1})$. The state-transition PDF for grid cells is modeled as $f(o_{i,n} | o_{i,n-1}) = \delta(o_{i,n} - o_{i,n-1})$ for stationary environment. In line with [15], [16], [27], the state-transition PDF $f(\underline{\mathbf{y}}_{s,n} | \underline{\mathbf{y}}_{s,n-1}) = f(\underline{\mathbf{p}}_{s,\text{sfv}}, \underline{\rho}_s, \underline{\mathbf{r}}_{s,n} | \mathbf{p}_{s,\text{sfv}}, \rho_s, r_{s,n-1})$ at PA $j = 1$ is defined as

$$f(\underline{\mathbf{p}}_{s,\text{sfv}}, \underline{\rho}_s, \underline{\mathbf{r}}_{s,n} | \mathbf{p}_{s,\text{sfv}}, \rho_s, 1)$$

$$= \begin{cases} (1 - p_s) f_D(\underline{\mathbf{p}}_{s,\text{sfv}}, \underline{\rho}_s), & \underline{\mathbf{r}}_{s,n} = 0 \\ p_s f(\underline{\mathbf{p}}_{s,\text{sfv}}, \underline{\rho}_s | \mathbf{p}_{s,\text{sfv}}, \rho_s), & \underline{\mathbf{r}}_{s,n} = 1 \end{cases} \quad (4)$$

for $r_{s,n-1} = 1$. For a nonexistent SFV at the previous time, i.e., $r_{s,n-1} = 0$, it is defined as

$$f(\underline{\mathbf{p}}_{s,\text{sfv}}, \underline{\rho}_s, \underline{\mathbf{r}}_{s,n} | \mathbf{p}_{s,\text{sfv}}, \rho_s, 0) = \begin{cases} f_D(\underline{\mathbf{p}}_{s,\text{sfv}}, \underline{\rho}_s), & \underline{\mathbf{r}}_{s,n} = 0 \\ 0, & \underline{\mathbf{r}}_{s,n} = 1. \end{cases} \quad (5)$$

To account for the sequential update, we further define $f(\underline{\mathbf{p}}_{s,\text{sfv}}, \underline{\rho}_s^{(j)}, \underline{\mathbf{r}}_{s,n}^{(j)} | \mathbf{p}_{s,\text{sfv}}^{(j-1)}, \rho_s^{(j-1)}, r_{s,n-1}^{(j-1)})$ for $j \geq 2$, which reads

$$f(\underline{\mathbf{p}}_{s,\text{sfv}}^{(j)}, \underline{\rho}_s^{(j)}, \underline{\mathbf{r}}_{s,n}^{(j)} | \mathbf{p}_{s,\text{sfv}}^{(j-1)}, \rho_s^{(j-1)}, 1)$$

$$= \begin{cases} f_D(\underline{\mathbf{p}}_{s,\text{sfv}}^{(j)}, \underline{\rho}_s^{(j)}), & \underline{\mathbf{r}}_{s,n}^{(j)} = 0 \\ f(\underline{\mathbf{p}}_{s,\text{sfv}}^{(j)}, \underline{\rho}_s^{(j)} | \mathbf{p}_{s,\text{sfv}}^{(j-1)}, \rho_s^{(j-1)}), & \underline{\mathbf{r}}_{s,n}^{(j)} = 1, \end{cases} \quad (6)$$

$$f(\underline{\mathbf{p}}_{s,\text{sfv}}^{(j)}, \underline{\rho}_s^{(j)}, \underline{\mathbf{r}}_{s,n}^{(j)} | \mathbf{p}_{s,\text{sfv}}^{(j-1)}, \rho_s^{(j-1)}, 0)$$

$$= \begin{cases} f_D(\underline{\mathbf{p}}_{s,\text{sfv}}^{(j)}, \underline{\rho}_s^{(j)}), & \underline{\mathbf{r}}_{s,n}^{(j)} = 0 \\ 0, & \underline{\mathbf{r}}_{s,n}^{(j)} = 1. \end{cases} \quad (7)$$

The PDF $f_D(\cdot)$ is an arbitrary ‘‘dummy PDF’’ to complete the statistics. The initial prior PDFs $f(\mathbf{x}_0)$, $f(\underline{\mathbf{y}}_{s,0})$ for $s \in \mathcal{S}_0$ and $f(\mathbf{o}_0)$ at time $n = 0$ are assumed to be known. Note that the initial prior PDF $f(\mathbf{o}_0)$ can be modeled as uniform when no prior knowledge of the RoI is available, or obtained from a established map generated by other agents or sensors.

$$\begin{aligned}
& f(\mathbf{x}_{0:n}, \mathbf{y}_{0:n}, \mathbf{o}_{0:n}, \underline{\mathbf{a}}_{1:n}, \bar{\mathbf{a}}_{1:n} \mid \mathbf{z}_{1:n}) \\
& \propto f(\mathbf{x}_0) \prod_{s=1}^{S_0} f(\mathbf{y}_{s,0}) \prod_{i=1}^Q f(o_{i,0}) \left(\prod_{n=1}^N f(\mathbf{x}_n \mid \mathbf{x}_{n-1}) f(o_n \mid o_{n-1}) \right) \prod_{s=1}^{S_n} f(\mathbf{y}_{s,n} \mid \mathbf{y}_{s,n-1}) \left(\prod_{j=2}^J \prod_{s=1}^{S_n^{(j)}} f(\mathbf{y}_{ss',n}^{(j)} \mid \mathbf{y}_{s,n-1}^{(j)}) \right) \\
& \times \prod_{m=1}^{M_n^{(j)}} \psi(a_{00,n}^{(j)}, \bar{a}_{m,n}^{(j)}) \prod_{j=1}^J q_{\text{P}}(\mathbf{x}_n, \underline{\mathbf{y}}_{0,n}^{(j)}, \mathbf{o}_n, \underline{a}_{00,n}^{(j)}; \mathbf{z}_n^{(j)}) \prod_{m'=1}^{M_n^{(j)}} \psi(a_{s',n}^{(j)}, \bar{a}_{m',n}^{(j)}) \prod_{s=1}^{S_n^{(j)}} q_{\text{S}}(\mathbf{x}_n, \underline{\mathbf{y}}_{s,n}^{(j)}, \mathbf{o}_n, \underline{a}_{ss',n}^{(j)}; \mathbf{z}_n^{(j)}) \\
& \times \prod_{m'=1}^{M_n^{(j)}} \psi(\underline{a}_{ss',n}^{(j)}, \bar{a}_{m',n}^{(j)}) \prod_{s=1, s \neq s'}^{S_n^{(j)}} q_{\text{D}}(\mathbf{x}_n, \underline{\mathbf{y}}_{s,n}^{(j)}, \underline{\mathbf{y}}_{s',n}^{(j)}, \mathbf{o}_n, \underline{a}_{ss',n}^{(j)}; \mathbf{z}_n^{(j)}) \prod_{m=1}^{M_n^{(j)}} \bar{q}_{\text{N}}(\mathbf{x}_n, \bar{\mathbf{y}}_{m,n}^{(j)}, \bar{a}_{m,n}^{(j)}; \mathbf{z}_n^{(j)}). \tag{3}
\end{aligned}$$

D. Data Association

Data association (DA) between measurements and PSFVs is represented by two complementary DA vectors: the *PSFV-oriented* association vector $\underline{\mathbf{a}}_n^{(j)} \triangleq [\underline{a}_{00,n}^{(j)} \underline{a}_{11,n}^{(j)} \cdots \underline{a}_{S_n^{(j)} S_n^{(j)},n}^{(j)}]^\text{T}$ and the *measurement-oriented* association vector $\bar{\mathbf{a}}_n^{(j)} \triangleq [\bar{a}_{1,n}^{(j)} \cdots \bar{a}_{M_n^{(j)},n}^{(j)}]^\text{T}$, see [16], [17], [27] for further details.

E. Factor Graph

Using Bayes' rule and independence assumptions related to the state-transition PDFs, the prior PDFs, and the LHF, the joint posterior PDF $f(\mathbf{x}_{0:n}, \mathbf{y}_{0:n}, \mathbf{o}_{0:n}, \underline{\mathbf{a}}_{1:n}, \bar{\mathbf{a}}_{1:n} \mid \mathbf{z}_{1:n})$ is given by (3), where the individual LHF related factors are introduced as follows.

For the *LoS path related to PA j* : the pseudo LHF $q_{\text{P}}(\mathbf{x}_n, \underline{\mathbf{y}}_{0,n}^{(j)}, \mathbf{o}_n, \underline{a}_{00,n}^{(j)}; \mathbf{z}_n^{(j)}) = q_{\text{P}}(\mathbf{x}_n, r_{0,n}^{(j)}, \mathbf{o}_n, \underline{a}_{00,n}^{(j)}; \mathbf{z}_n^{(j)})$ is given by

$$\begin{aligned}
& q_{\text{P}}(\mathbf{x}_n, r_{0,n}^{(j)} = 1, \mathbf{o}_n, \underline{a}_{00,n}^{(j)}; \mathbf{z}_n^{(j)}) \\
& \triangleq \begin{cases} \frac{f_{\text{P}}(\mathbf{z}_{m,n}^{(j)} \mid \mathbf{p}_n, u_{00,n}^{(j)}) p_{\text{d},00}^{(j)}}{\mu_{\text{fa}} f_{\text{fa}}(\mathbf{z}_{m,n}^{(j)})}, & \underline{a}_{00,n}^{(j)} \in \mathcal{M}_n^{(j)} \\ 1 - p_{\text{d},00}^{(j)}, & \underline{a}_{00,n}^{(j)} = 0. \end{cases} \tag{8}
\end{aligned}$$

for the case $\mathbf{o}_n \in \mathcal{V}_{0,n}^{(j)}$, and $q_{\text{P}}(\mathbf{x}_n, r_{0,n}^{(j)} = 0, \mathbf{o}_n, \underline{a}_{00,n}^{(j)}; \mathbf{z}_n^{(j)}) \triangleq \delta(\underline{a}_{00,n}^{(j)})$ for $\mathbf{o}_n \in \mathcal{Q}$.

For *single-bounce paths related to PA j* : $(s, s) \in \mathcal{D}_{\text{S},n}^{(j)}$, the pseudo LHF $q_{\text{S}}(\mathbf{x}_n, \underline{\mathbf{y}}_{s,n}^{(j)}, \mathbf{o}_n, \underline{a}_{ss,n}^{(j)}; \mathbf{z}_n^{(j)}) = q_{\text{S}}(\mathbf{x}_n, \underline{\mathbf{p}}_{s,\text{sfv}}^{(j)}, r_{s,n}^{(j)}, \rho_s^{(j)}, \mathbf{o}_n, \underline{a}_{ss,n}^{(j)}; \mathbf{z}_n^{(j)})$ is given by

$$\begin{aligned}
& q_{\text{S}}(\mathbf{x}_n, \underline{\mathbf{p}}_{s,\text{sfv}}^{(j)}, r_{s,n}^{(j)} = 1, \rho_s^{(j)}, \mathbf{o}_n, \underline{a}_{ss,n}^{(j)}; \mathbf{z}_n^{(j)}) \\
& \triangleq \begin{cases} \frac{f_{\text{S}}(\mathbf{z}_{m,n}^{(j)} \mid \mathbf{p}_n, \underline{\mathbf{p}}_{s,\text{sfv}}^{(j)}, u_{ss,n}^{(j)}) p_{\text{d},ss}^{(j)}}{\mu_{\text{fa}} f_{\text{fa}}(\mathbf{z}_{m,n}^{(j)})}, & \underline{a}_{ss,n}^{(j)} \in \mathcal{M}_n^{(j)} \\ 1 - p_{\text{d},ss}^{(j)}, & \underline{a}_{ss,n}^{(j)} = 0 \end{cases} \tag{9}
\end{aligned}$$

for the case $\mathbf{o}_n \in \mathcal{V}_{ss,n}^{(j)}$, and $q_{\text{S}}(\mathbf{x}_n, \underline{\mathbf{p}}_{s,\text{sfv}}^{(j)}, r_{s,n}^{(j)} = 0, \rho_s^{(j)}, \mathbf{o}_n, \underline{a}_{ss,n}^{(j)}; \mathbf{z}_n^{(j)}) \triangleq \delta(\underline{a}_{ss,n}^{(j)})$ for $\mathbf{o}_n \in \mathcal{Q}$.

For *double-bounce paths related to (s, s')* : $(s, s') \in \mathcal{D}_{\text{D},n}^{(j)}$: the pseudo LHF $q_{\text{D}}(\mathbf{x}_n, \underline{\mathbf{y}}_{s,n}^{(j)}, \underline{\mathbf{y}}_{s',n}^{(j)}, \mathbf{o}_n, \underline{a}_{ss',n}^{(j)}; \mathbf{z}_n^{(j)}) = q_{\text{D}}(\mathbf{x}_n, \underline{\mathbf{p}}_{s,\text{sfv}}^{(j)}, r_{s,n}^{(j)}, \rho_s^{(j)}, \underline{\mathbf{p}}_{s',\text{sfv}}^{(j)}, r_{s',n}^{(j)}, \rho_{s'}^{(j)}, \mathbf{o}_n, \underline{a}_{ss',n}^{(j)}; \mathbf{z}_n^{(j)})$ is given by

$$q_{\text{D}}(\mathbf{x}_n, \underline{\mathbf{p}}_{s,\text{sfv}}^{(j)}, r_{s,n}^{(j)} = 1, \rho_s^{(j)}, \underline{\mathbf{p}}_{s',\text{sfv}}^{(j)}, r_{s',n}^{(j)} = 1, \rho_{s'}^{(j)}, \mathbf{o}_n, \underline{a}_{ss',n}^{(j)}; \mathbf{z}_n^{(j)})$$

$$\triangleq \begin{cases} f_{\text{D}}(\mathbf{z}_{m,n}^{(j)} \mid \mathbf{p}_n, \underline{\mathbf{p}}_{s,\text{sfv}}^{(j)}, \underline{\mathbf{p}}_{s',\text{sfv}}^{(j)}, u_{ss',n}^{(j)}) \\ \times \frac{p_{\text{d},ss'}^{(j)}}{\mu_{\text{fa}} f_{\text{fa}}(\mathbf{z}_{m,n}^{(j)})}, & \underline{a}_{ss',n}^{(j)} \in \mathcal{M}_n^{(j)} \\ 1 - p_{\text{d},ss'}^{(j)}, & \underline{a}_{ss',n}^{(j)} = 0 \end{cases} \tag{10}$$

for the case $\mathbf{o}_n \in \mathcal{V}_{ss',n}^{(j)}$, otherwise $q_{\text{D}}(\cdots) \triangleq \delta(\underline{a}_{ss',n}^{(j)})$ for $\mathbf{o}_n \in \mathcal{Q}$.

For *new paths*: we assume that the new path is independent of the grid cell states, the pseudo LHF $\bar{q}_{\text{N}}(\mathbf{x}_n, \bar{\mathbf{y}}_{m,n}^{(j)}, \bar{a}_{m,n}^{(j)}; \mathbf{z}_n^{(j)}) = \bar{q}_{\text{N}}(\mathbf{x}_n, \bar{\mathbf{p}}_{m,\text{sfv}}^{(j)}, \bar{r}_{m,n}^{(j)} = 1, \bar{\rho}_m^{(j)}, \bar{a}_{m,n}^{(j)}; \mathbf{z}_n^{(j)})$ is given by

$$\begin{aligned}
& \bar{q}_{\text{N}}(\mathbf{x}_n, \bar{\mathbf{p}}_{m,\text{sfv}}^{(j)}, \bar{r}_{m,n}^{(j)} = 1, \bar{\rho}_m^{(j)}, \bar{a}_{m,n}^{(j)}; \mathbf{z}_n^{(j)}) \\
& \triangleq \begin{cases} 0, & \bar{a}_{m,n}^{(j)} \in \tilde{\mathcal{D}}_n^{(j)} \\ f_{\text{N}}(\mathbf{z}_{m,n}^{(j)} \mid \mathbf{p}_n, \bar{\mathbf{p}}_{m,\text{sfv}}^{(j)}, \bar{u}_{m,n}^{(j)}) \\ \times \frac{\mu_{\text{N}} f_{\text{N}}(\bar{\mathbf{p}}_{m,\text{sfv}}^{(j)}, \bar{\rho}_m^{(j)} \mid \mathbf{x}_n)}{\mu_{\text{fa}} f_{\text{fa}}(\mathbf{z}_{m,n}^{(j)})}, & \bar{a}_{m,n}^{(j)} = 0 \end{cases} \tag{11}
\end{aligned}$$

and $\bar{q}_{\text{N}}(\mathbf{x}_n, \bar{\mathbf{p}}_{m,\text{sfv}}^{(j)}, \bar{r}_{m,n}^{(j)} = 0, \bar{\rho}_m^{(j)}, \bar{a}_{m,n}^{(j)}; \mathbf{z}_n^{(j)}) \triangleq f_{\text{D}}(\bar{\mathbf{p}}_{m,\text{sfv}}^{(j)}, \bar{\rho}_m^{(j)})$.

F. Detection and State Estimation

Using all measurements up to time n , we sequentially detect PSFVs based on the marginal posterior existence probabilities $f(r_{s,n} = 1 \mid \mathbf{z}_{1:n}) = \int f(\mathbf{p}_{s,\text{sfv}}, \rho_s, r_{s,n} = 1 \mid \mathbf{z}_{1:n}) d\mathbf{p}_{s,\text{sfv}} d\rho_s$. A PSFV is declared to exist (i.e., detected) if $f(r_{s,n} = 1 \mid \mathbf{z}_{1:n}) > p_{\text{sfv}}$, where p_{sfv} is the existence probability threshold. Since introducing new PSFVs causes the number of PSFVs to grow with time n , PSFVs with existence probabilities below a threshold p_{pr} are removed from the state space ("pruned"). We determine the minimum mean-square error (MMSE) estimate by calculating the marginal posterior PDFs $f(\mathbf{p}_{s,\text{sfv}} \mid r_{s,n} = 1, \mathbf{z}_{1:n}) = (\int f(\mathbf{p}_{s,\text{sfv}}, \rho_s, r_{s,n} = 1 \mid \mathbf{z}_{1:n}) d\rho_s) / f(r_{s,n} = 1 \mid \mathbf{z}_{1:n})$ and $f(\rho_s \mid r_{s,n} = 1, \mathbf{z}_{1:n})$ and $f(o_{i,n} \mid \mathbf{z}_{1:n})$. The marginal posterior PDFs cannot be obtained analytically by direct marginalization of (3), therefore we perform sequential message-passing by means of SPA on a factor graph to obtain approximations (beliefs) of these marginal posterior PDFs, for instance, $\tilde{f}(o_{i,n})$ is obtained as an approximation of $f(o_{i,n} \mid \mathbf{z}_{1:n})$.

G. Selected SPA Messages

Due to page limit, the full derivation of all SPA messages is omitted, and only the key messages relevant to the cell states

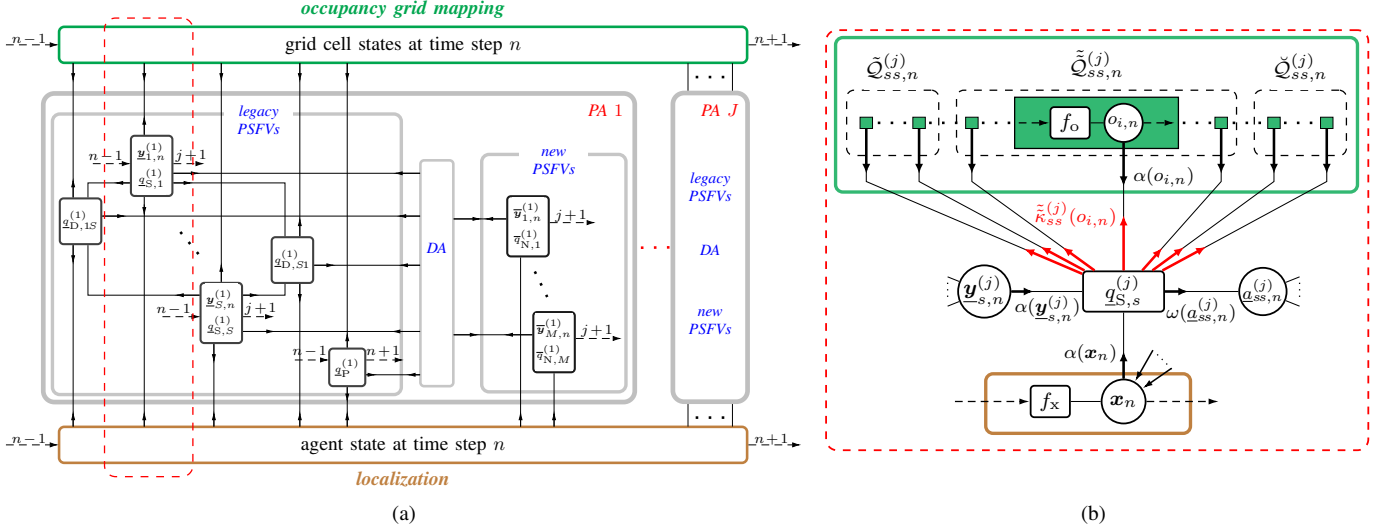


Fig. 2: Factor graph representation of the joint posterior PDF (3). (a) shows the message propagation between the subgraphs, as well as iterations over time and PAs. The black square and circle symbols denote factor nodes and variable nodes, respectively. Dashed arrows indicate messages propagated forward in time. As an example, (b) shows the variable nodes, factor nodes, and messages for a single-bounce path. The following short notations are used: $S \triangleq S_n^{(j)}$, $M \triangleq M_n^{(j)}$, $f_x \triangleq f(\mathbf{x}_n | \mathbf{x}_{n-1})$, $f_o \triangleq f(o_{i,n} | o_{i,n-1})$, $q_P^{(j)}$, $q_{S,s}^{(j)}$, $q_{D,ss'}^{(j)}$ and $q_{N,m}^{(j)}$ represent the pseudo LHF of the LoS paths (8), single-bounce paths (9), double-bounce paths (10) and new paths (11), respectively.

are presented. For all legacy PSFVs $s \in \mathcal{S}_{n-1}$, the predicted messages $\alpha(\underline{\mathbf{y}}_{s,n}) = \alpha(\underline{\mathbf{p}}_{s,\text{sfv}}, r_{s,n}, \rho_s)$ are given by

$$\begin{aligned} & \alpha(\underline{\mathbf{p}}_{s,\text{sfv}}, r_{s,n}, \rho_s) \\ &= \sum_{r_{s,n-1} \in \{0,1\}} \int f(\underline{\mathbf{p}}_{s,\text{sfv}}, r_{s,n}, \rho_s | \underline{\mathbf{p}}_{s,\text{sfv}}, r_{s,n-1}, \rho_s) \\ & \quad \times \tilde{f}(\underline{\mathbf{p}}_{s,\text{sfv}}, r_{s,n-1}, \rho_s) d\underline{\mathbf{p}}_{s,\text{sfv}} d\rho_s. \end{aligned} \quad (12)$$

For all grid cells, the predicted messages are given by

$$\alpha(o_{i,n}) = \sum_{o_{i,n-1}} f(o_{i,n} | o_{i,n-1}) \tilde{f}(o_{i,n-1}). \quad (13)$$

We further define $\alpha_{\mathcal{V}_{ss',n}^{(j)}}$ according to (1) as

$$\alpha_{\mathcal{V}_{ss',n}^{(j)}} = \left(\prod_{i \in \mathcal{Q}_{ss',n}^{(j)}} \alpha(o_{i,n} = 0) \right) \left(1 - \prod_{i' \in \tilde{\mathcal{Q}}_{ss',n}^{(j)}} (1 - \alpha(o_{i',n} = 1)) \right). \quad (14)$$

1) *Measurement Evaluation for LoS Paths:* The messages $\omega(\underline{\mathbf{a}}_{00,n}^{(j)})$ propagate from the j th PA related factor node $q_P(\mathbf{x}_n, \underline{\mathbf{y}}_{0,n}^{(j)}, \mathbf{o}_n, \underline{\mathbf{a}}_{00,n}^{(j)}; \mathbf{z}_n^{(j)})$ to the feature-oriented association variable nodes $\underline{\mathbf{a}}_{00,n}^{(j)}$ are given by

$$\begin{aligned} \omega(\underline{\mathbf{a}}_{00,n}^{(j)}) &= \int \underbrace{\alpha(\mathbf{x}_n) \alpha_{\mathcal{V}_{00,n}^{(j)}}}_{R_{00,n}^{(j)}} q_P(\mathbf{x}_n, r_{0,n}^{(j)} = 1, \mathbf{o}_n, \underline{\mathbf{a}}_{00,n}^{(j)}; \mathbf{z}_n^{(j)}) \\ & \quad \times \underbrace{\alpha(\underline{\mathbf{p}}_{0,\text{sfv}}^{(j)}, r_{s,n}^{(j)} = 1, \rho_0^{(j)})}_{\bar{R}_{00,n}^{(j)}} d\mathbf{x}_n + \underbrace{1(\underline{\mathbf{a}}_{00,n}^{(j)}) \alpha_{0,n}^{(j)}}_{\bar{R}_{00,n}^{(j)}} \end{aligned} \quad (15)$$

where $\alpha(\mathbf{x}_n)$ denotes the agent predicted message, and $\alpha_{s,n}^{(j)}$ is related to the nonexistence probability of PSFV s .

2) *Measurement Evaluation for Legacy PSFVs:*

a) *Single-Bounce Propagation Path:* For $s = s'$, the messages $\omega(\underline{\mathbf{a}}_{ss,n}^{(j)})$ propagate from the single-bounce potential ray (PR) related factor node $q_S(\mathbf{x}_n, \underline{\mathbf{y}}_{s,n}^{(j)}, \mathbf{o}_n, \underline{\mathbf{a}}_{ss,n}^{(j)}; \mathbf{z}_n^{(j)})$ to the feature-oriented association variable nodes $\underline{\mathbf{a}}_{ss,n}^{(j)}$ and are given by

$$\begin{aligned} \omega(\underline{\mathbf{a}}_{ss,n}^{(j)}) &= \underbrace{\iiint \alpha(\mathbf{x}_n) \alpha_{\mathcal{V}_{ss,n}^{(j)}}}_{R_{ss,n}^{(j)}} \alpha(\underline{\mathbf{p}}_{s,\text{sfv}}^{(j)}, r_{s,n}^{(j)} = 1, \rho_s^{(j)}) \\ & \quad \underbrace{q_P(\mathbf{x}_n, \underline{\mathbf{p}}_{s,\text{sfv}}^{(j)}, r_{s,n}^{(j)} = 1, \rho_s^{(j)}, \mathbf{o}_n, \underline{\mathbf{a}}_{ss,n}^{(j)}; \mathbf{z}_n^{(j)})}_{\bar{R}_{ss,n}^{(j)}} d\mathbf{x}_n d\underline{\mathbf{p}}_{s,\text{sfv}}^{(j)} d\rho_s^{(j)} \\ & \quad + \underbrace{1(\underline{\mathbf{a}}_{ss,n}^{(j)}) \alpha_{s,n}^{(j)}}_{\bar{R}_{ss,n}^{(j)}}. \end{aligned} \quad (16)$$

b) *Double-Bounce Propagation Path:* For $s \neq s'$, the messages $\omega(\underline{\mathbf{a}}_{ss',n}^{(j)})$ propagate from the double-bounce PR related factor node $q_D(\mathbf{x}_n, \underline{\mathbf{y}}_{s,n}^{(j)}, \underline{\mathbf{y}}_{s',n}^{(j)}, \mathbf{o}_n, \underline{\mathbf{a}}_{ss',n}^{(j)}; \mathbf{z}_n^{(j)})$ to the feature-oriented association variable nodes $\underline{\mathbf{a}}_{ss',n}^{(j)}$ given by

$$\begin{aligned} \omega(\underline{\mathbf{a}}_{ss',n}^{(j)}) &= \underbrace{\int \cdots \int \alpha(\mathbf{x}_n) \alpha_{\mathcal{V}_{ss',n}^{(j)}}}_{R_{ss',n}^{(j)}} \alpha(\underline{\mathbf{p}}_{s,\text{sfv}}^{(j)}, r_{s,n}^{(j)} = 1, \rho_s^{(j)}) \\ & \quad \times \underbrace{\alpha(\underline{\mathbf{p}}_{s',\text{sfv}}^{(j)}, r_{s',n}^{(j)} = 1, \rho_{s'}^{(j)})}_{R_{ss',n}^{(j)}} q_D(\mathbf{x}_n, \underline{\mathbf{p}}_{s,\text{sfv}}^{(j)}, r_{s,n}^{(j)} = 1, \rho_s^{(j)}, \underline{\mathbf{p}}_{s',\text{sfv}}^{(j)}, \\ & \quad \underbrace{r_{s',n}^{(j)} = 1, \rho_{s'}^{(j)}, \mathbf{o}_n, \underline{\mathbf{a}}_{ss',n}^{(j)}; \mathbf{z}_n^{(j)}}_{R_{ss',n}^{(j)}} d\mathbf{x}_n d\underline{\mathbf{p}}_{s,\text{sfv}}^{(j)} d\rho_s^{(j)} d\underline{\mathbf{p}}_{s',\text{sfv}}^{(j)} d\rho_{s'}^{(j)} \\ & \quad + \underbrace{1(\underline{\mathbf{a}}_{ss',n}^{(j)}) \left(\alpha_{s,n}^{(j)} \int \alpha(\underline{\mathbf{p}}_{s',\text{sfv}}^{(j)}, r_{s',n}^{(j)} = 1, \rho_{s'}^{(j)}) d\underline{\mathbf{p}}_{s',\text{sfv}}^{(j)} d\rho_{s'}^{(j)} \right)}_{\bar{R}_{ss',n}^{(j)}} \\ & \quad + \underbrace{\alpha_{s',n}^{(j)} \int \alpha(\underline{\mathbf{p}}_{s,\text{sfv}}^{(j)}, r_{s,n}^{(j)} = 1, \rho_s^{(j)}) d\underline{\mathbf{p}}_{s,\text{sfv}}^{(j)} d\rho_s^{(j)} + \alpha_{s,n}^{(j)} \alpha_{s',n}^{(j)}}_{\bar{R}_{ss',n}^{(j)}}. \end{aligned} \quad (17)$$

3) *Measurement Update for Grid Cells*: For the update of the states of the grid cells, only the messages from the legacy PSFVs are used. The messages $\tilde{\kappa}_{ss'}^{(j)}(o_{i,n})$, $\tilde{\kappa}_{ss'}^{(j)}(o_{i,n})$ and $\tilde{\kappa}_{ss'}^{(j)}(o_{i,n})$ with $(s, s') \in \tilde{\mathcal{D}}_n^{(j)}$ sent from the factor node $q_P(\dots)$, $q_S(\dots)$ or $q_D(\dots)$ to the cell state $o_{i,n}$ are given as follows. If this cell is traversed by the ray, i.e., $i \in \tilde{\mathcal{Q}}_{ss',n}^{(j)}$,

$$\begin{aligned} \tilde{\kappa}_{ss'}^{(j)}(o_{i,n} = 0) &= \sum_{\underline{a}_{ss',n}^{(j)} \in \mathcal{M}_{0,n}^{(j)}} \eta(\underline{a}_{ss',n}^{(j)})(R_{ss',n}^{(j)}/\alpha(o_{i,n} = 0)) \\ &+ \eta(\underline{a}_{ss',n}^{(j)} = 0)\bar{R}_{ss',n}^{(j)}, \end{aligned} \quad (18)$$

$$\text{and } \tilde{\kappa}_{ss'}^{(j)}(o_{i,n} = 1) = \eta(\underline{a}_{ss',n}^{(j)} = 0)\bar{R}_{ss',n}^{(j)}.$$

If this cell is part of the interacting surface, i.e., $i \in \tilde{\mathcal{Q}}_{ss',n}^{(j)}$,

$$\begin{aligned} \tilde{\kappa}_{ss'}^{(j)}(o_{i,n} = 1) &= \sum_{\underline{a}_{ss',n}^{(j)} \in \mathcal{M}_{0,n}^{(j)}} \eta(\underline{a}_{ss',n}^{(j)})(R_{ss',n}^{(j)}/\alpha(o_{i,n} = 1)) \\ &+ \eta(\underline{a}_{ss',n}^{(j)} = 0)\bar{R}_{ss',n}^{(j)}, \end{aligned} \quad (19)$$

$$\text{and } \tilde{\kappa}_{ss'}^{(j)}(o_{i,n} = 0) = \eta(\underline{a}_{ss',n}^{(j)} = 0)\bar{R}_{ss',n}^{(j)}.$$

If this cell is not interacted with this ray $i \in \tilde{\mathcal{Q}}_{k,n}^{(j)}$, we still formulate the update to maintain complete statistics, yields

$$\tilde{\kappa}_{ss'}^{(j)}(o_{i,n}) = \sum_{\underline{a}_{ss',n}^{(j)} \in \mathcal{M}_{0,n}^{(j)}} \eta(\underline{a}_{ss',n}^{(j)})R_{ss',n}^{(j)} + \eta(\underline{a}_{ss',n}^{(j)} = 0)\bar{R}_{ss',n}^{(j)}. \quad (20)$$

4) *Belief Calculation*: After calculating the messages for all PAs, the beliefs that approximate $f(o_{i,n} | z_{1:n})$ are given by

$$\tilde{f}(o_{i,n}) = C_o \alpha(o_{i,n}) \prod_{j=1}^J \prod_{(s,s') \in \tilde{\mathcal{D}}_n^{(j)}} \tilde{\kappa}_{ss'}^{(j)}(o_{i,n}) \tilde{\kappa}_{ss'}^{(j)}(o_{i,n}) \tilde{\kappa}_{ss'}^{(j)}(o_{i,n}) \quad (21)$$

where the normalization constant C_o ensures that the belief is a valid probability distribution.

H. Implementation Aspect

In particle-based implementations, the evaluation of particle-grid interactions and the calculation of associated statistical updates are computationally intensive. While particle independence enables efficient parallelization, careful aggregation across particles and propagation paths along with normalization is crucial for maintaining numerical stability and probabilistic consistency. In particular, for each propagation path, the relevant statistics are first integrated over all particles before combining information across paths and PAs in (21).

IV. RESULTS

The performance of the proposed algorithm is validated using synthetic radio measurements generated in a challenging environment, as shown in Fig. 3a, which could represent a complex indoor environment or an outdoor urban street canyon. This environment consists of three PAs and features geometrically complex and nonconvex structures with concrete walls and glass windows, characterized by reflection coefficients of $\rho_s = 0.5$ and $\rho_s = 0.8$, respectively. Agent 1 and

agent 2 explore the RoI sequentially. The following simulation setup and parameters are used.

A. Analysis Setup

The state-transition PDF $f(\beta_n | \beta_{n-1})$ of the agent is defined by a linear near constant-velocity motion model [28] as $\beta_n = \mathbf{F}\beta_{n-1} + \mathbf{\Gamma}\nu_n$, where the transition matrices $\mathbf{F} \in \mathbb{R}^{4 \times 4}$ and $\mathbf{\Gamma} \in \mathbb{R}^{4 \times 2}$ are chosen as in [28]. The driving process $\nu_n \in \mathbb{R}^{2 \times 1}$ is independent and identically distributed (iid) over time n , zero-mean and Gaussian with covariance matrix $\sigma_\nu^2 \mathbf{I}_2$. The state-transition PDF of the agent's orientation is given as $\Delta\varphi_n = \Delta\varphi_{n-1} + \epsilon_{\varphi,n}$ where the noise $\epsilon_{\varphi,n}$ is zero-mean and Gaussian with variance σ_φ^2 . The state-transition PDF of the positions of legacy PSFV $\underline{p}_{s,\text{sfv}}$ is chosen to be $\underline{p}_{s,\text{sfv}} = \mathbf{p}_{s,\text{sfv}} + \epsilon_{s,n}$, where the noise $\epsilon_{s,n}$ is iid, zero-mean Gaussian across j and n , with variance $\sigma_{p_s}^2 \mathbf{I}_2$. The state-transition PDF of the surface reflection coefficient $\underline{\rho}_{s,n}$ is chosen to be $\underline{\rho}_{s,n} = \rho_s + \epsilon_{\rho_s}$, where the noise ϵ_{ρ_s} is iid across s , zero-mean, and Gaussian with variance σ_ρ^2 . The state-transition model of the grid cell states is given as $o_{i,n} = o_{i,n-1}$. We performed simulation with the following parameters: the detection threshold for normalized amplitude measurements $u_{\text{de}} = 6$ dB, the variance of the agent acceleration noise $\sigma_\nu^2 = 9 \cdot 10^{-4} \text{ m/s}^2$, the orientation noise STD $\sigma_\varphi = 2^\circ$, the regularization noise STD for PSFV positions $\sigma_{p_s} = 0.01 \text{ m}$, the STD for the reflection coefficient $\sigma_\rho = 0.01$.

The samples for the initial agent state are drawn from a 5-D uniform distribution centered at $[\mathbf{p}_0^T \ 0 \ 0 \ \Delta\varphi_0]^T$ where \mathbf{p}_0 and $\Delta\varphi_0$ are the true agent start position and orientation, and the support of position, velocity and orientation components are $[-0.5, 0.5] \text{ m}$, $[0.01, 0.01] \text{ m/s}$ and $[-5^\circ, 5^\circ]$, respectively. The samples representing the initial state of the new PSFVs $\mathbf{p}_{\text{sfv}}^{\text{ini}}$ are drawn from the PDF $f(\mathbf{p}_{\text{sfv}}^{\text{ini}})$ which is uniform in RoI, i.e., $[-15\text{m}, 15\text{m}] \times [-15\text{m}, 15\text{m}]$ centered at the coordinate center. For any new PSFVs, it is assumed that the initial state of the reflection coefficient ρ_m^{ini} is uniform on $[0.1, 0.9]$. The mean number of new PSFVs is $\mu_n = 0.05$, the survival probability is $p_s = 0.99$, the detection and pruning threshold are $p_{\text{de}} = 0.5$ and $p_{\text{pr}} = 0.1$, and the PDFs of the states of the random variables are represented by 13000 particles each.

B. Synthetic Measurements

We synthetically generate the measurements $z_{m,n}^{(j)}$ according to the scenario shown in Fig. 3a, where a D-MIMO system operating at $f_c = 6 \text{ GHz}$ with a bandwidth of 1 GHz is used. For the three PAs and two mobile agents, the same 5×5 uniform rectangular array with an inter-element spacing of $\lambda/4$ is used. Over time steps, time-varying distances, AoAs, AoDs, and normalized amplitudes were synthesized for propagation paths experiencing up to double surface reflections. The amplitude of each path is assumed to follow free-space pathloss and is attenuated by the reflection coefficient ρ_s after each surface reflection. Noisy measurements that account for non-ideal channel estimation and detection are obtained by adding noise to the true path parameters and stacked in the vector $z_n^{(j)}$, where the noise statistics are determined via Fisher information matrix [29]–[31] with $\text{SNR}_{1\text{m}} = 30 \text{ dB}$, the output SNR at 1 m from each PA. In addition, the false alarm (FA)

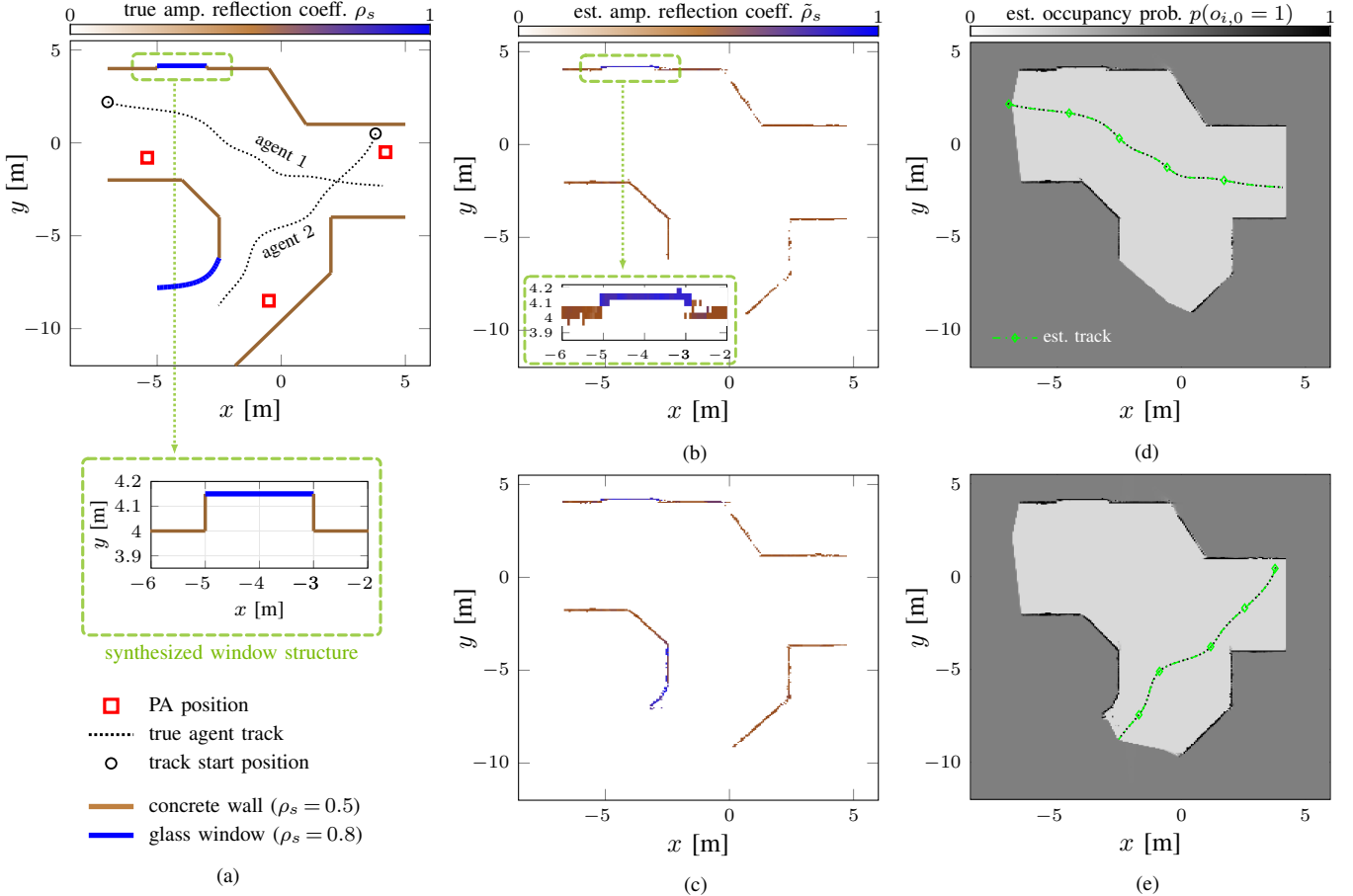


Fig. 3: Performance results using synthetic D-MIMO measurements. (a) Geometrical depiction of the simulation environment and setup. (b) and (d) show the localization and mapping results for agent 1. (c) and (e) present the results for agent 2 using the established occupancy grid map from agent 1 in (d) as prior for $p(o_0)$.

measurements are further added to $z_n^{(j)}$ with mean number $\mu_{fa} = 1$. Agent 1 follows a trajectory of 250 time steps and agent 2 of 230 time steps, with a step size of 5 cm. For modeling the occupancy probability of the environment, the RoI that spans $14.5\text{m} \times 17.5\text{m}$ is divided into square cells with side lengths of 0.06 m, resulting in $Q = 70664$ grid cells. All cells are initialized with a uniform prior with $p(o_{i,0} = 1) = 0.5 \forall i \in Q$ representing an unknown status that has not been explored, and a lower threshold of 0.15 is applied to facilitate rapid detection of objects in the estimated free area. Based on the PSFV and agent states, the path states are obtained and represented by 13000 particles (i.e., individual rays). Parallel ray casting is performed to determine ray–cell interactions, implemented in Taichi (Python) [32].

C. Result

Using synthetic measurements, we evaluate (i) localization performance, (ii) mapping performance assessed via reconstructed geometry, estimated material properties (captured by the reflection coefficients), and the ability to incrementally expand and update an existing map, and (iii) “soft” ray tracing, i.e., tracking specular propagation paths along with their geometric parameters, amplitudes, and associated variances. Starting from a uniform prior (i.e., without environmental knowledge), the agent 1 first explores the RoI to construct

an initial map. Agent 2 then uses this established map to continue exploration and refine reconstruction. The estimated reflection coefficients $\tilde{\rho}_s$ are shown in Figs. 3b and 3c for agents 1 and 2, respectively, where $\tilde{\rho}_s$ is projected onto grid cells with occupancy probabilities exceeding the initial value of 0.5. The resulting RF-related material maps, together with the occupancy reconstructions in Figs. 3d and 3e, accurately recover the geometry of the environment, including fine structures such as the window and the curved glass wall, and their RF-related properties. Moreover, Figs. 3d and 3e demonstrate the accurate agent localization performance of the proposed algorithm, achieving average position and orientation errors of 0.6 cm and 0.27° for agent 1 and 0.7 cm and 0.33° for agent 2.

The “soft” ray tracing results in Fig. 4 illustrate the path-level output of the proposed algorithm using measurements for agent 1. The estimated surfaces, obtained from the MMSE estimates of the PSFVs, closely match the groundtruth geometry, and the specular propagation paths are accurately detected and estimated, including their amplitudes. Unlike previous work [17] that modeled and inferred per-path existence and amplitude states, the proposed approach infers path geometry and amplitudes directly from the PSFV estimates and provides Fisher information-based variances. Such path-

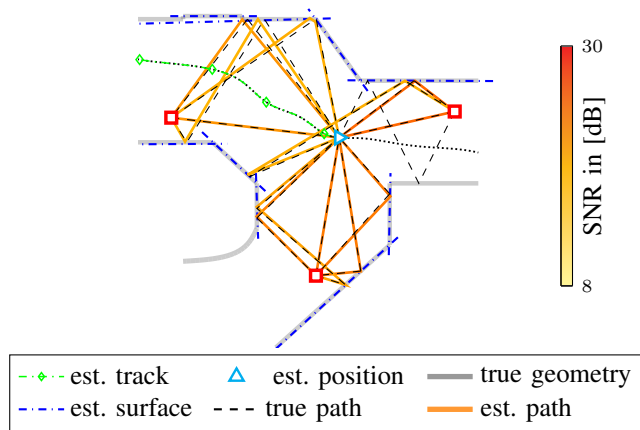


Fig. 4: Results of a simulation run for agent 1. The estimated surfaces, propagation paths and agent track are shown for time $n = 173$. The estimated surfaces are computed using the MMSE estimates of the detected SFVs. Estimated propagation paths are obtained by connecting the MMSE estimates of the agent position, interaction points on the estimated surfaces and PAs, and compared with the true visible paths. The color of each estimated path represents its SNR estimates, i.e., the square of norm amplitude estimates.

level information is useful beyond sensing, e.g., to support communications, facilitate channel prediction, beamforming and beam alignment.

V. CONCLUSION

This paper presented a probabilistic occupancy grid framework for radio-based localization and mapping, enabling the reconstruction of complex environment geometries together with their radio-related properties. The proposed approach jointly estimates the occupancy states of the grid cells, the reflection coefficients characterizing material properties, and the positions of the agents. The simulation results demonstrate accurate geometry and material reconstruction as well as high localization accuracy. Possible future research directions include extending the proposed framework to more realistic signal models, diverse feature models beyond planar surfaces, and to applications like passive localization.

REFERENCES

- [1] N. González-Prelcic *et al.*, “The integrated sensing and communication revolution for 6G: Vision, techniques, and applications,” *Proc. IEEE*, vol. 112, no. 7, pp. 676–723, May 2024.
- [2] H. Kim, K. Granstrom, L. Svensson, S. Kim, and H. Wymeersch, “PMBM-based SLAM filters in 5G mmWave vehicular networks,” *IEEE Trans. Veh. Technol.*, pp. 1–1, May 2022.
- [3] X. Li, X. Cai, E. Leitinger, and F. Tufvesson, “A belief propagation algorithm for multipath-based SLAM with multiple map features: A mmWave MIMO application,” in *Proc. IEEE ICC 2024*, Aug. 2024, pp. 269–275.
- [4] Y. Ge, O. Kaltiokallio, Y. Xia, A. F. García-Fernández, H. Kim, J. Talvitie, M. Valkama, H. Wymeersch, and L. Svensson, “Batch SLAM with PMBM data association sampling and graph-based optimization,” *IEEE Trans. Signal Process.*, vol. 73, pp. 2139–2153, May 2025.
- [5] M. Liang, E. Leitinger, and F. Meyer, “Direct multipath-based SLAM,” *IEEE Trans. Signal Process.*, vol. 74, Mar. 2025.
- [6] S. Thrun, “Learning occupancy grid maps with forward sensor models,” *Autonomous Robots*, vol. 15, pp. 111–127, Sept. 2003.
- [7] V. Dhiman, A. Kundu, F. Dellaert, and J. J. Corso, “Modern MAP inference methods for accurate and fast occupancy grid mapping on higher order factor graphs,” in *IEEE Int. Conf. Robot. Autom. (ICRA)*, Sept. 2014, pp. 2037–2044.

- [8] D. Nuss, S. Reuter, M. Thom, T. Yuan, G. Krehl, M. Maile, A. Gern, and K. Dietmayer, “A random finite set approach for dynamic occupancy grid maps with real-time application,” *Int. J. Robot. Res.*, vol. 37, pp. 841–866, Jul. 2018.
- [9] Y. Kwon, D. Kim, I. An, and S.-e. Yoon, “Super rays and culling region for real-time updates on grid-based occupancy maps,” *IEEE Trans. Robot.*, vol. 35, no. 2, pp. 482–497, Apr. 2019.
- [10] K. S. Shankar and N. Michael, “MRFFMap: Online probabilistic 3D mapping using forward ray sensor models,” in *Robotics: Science and Systems*, Jul. 2020.
- [11] C. Robbiano, E. K. P. Chong, M. R. Azimi-Sadjadi, L. L. Scharf, and A. Pezeshki, “Bayesian learning of occupancy grids,” *IEEE Trans. Intell. Transp. Syst.*, vol. 23, no. 2, pp. 1073–1084, Sept. 2022.
- [12] A. T. Irish, J. T. Isaacs, F. Quatin, J. a. P. Hespanha, and U. Madhok, “Belief propagation based localization and mapping using sparsely sampled GNSS SNR measurements,” in *Proc. IEEE Int. Conf. Robot. Autom. (ICRA)*, Sept. 2014, pp. 1977–1982.
- [13] G. Steinböck *et al.*, “Hybrid model for reverberant indoor radio channels using rays and graphs,” *IEEE Trans. Antennas Propag.*, vol. 64, no. 9, pp. 4036–4048, Sept. 2016.
- [14] Z. Li, F. Jiang, H. Wymeersch, and F. Wen, “An iterative 5G positioning and synchronization algorithm in NLOS environments with multi-bounce paths,” *IEEE Wireless Commun. Lett.*, vol. 12, no. 5, pp. 804–808, Feb. 2023.
- [15] E. Leitinger, F. Meyer, F. Hlawatsch, K. Witrals, F. Tufvesson, and M. Z. Win, “A belief propagation algorithm for multipath-based SLAM,” *IEEE Trans. Wireless Commun.*, vol. 18, no. 12, pp. 5613–5629, Dec. 2019.
- [16] E. Leitinger, A. Venus, B. Teague, and F. Meyer, “Data fusion for multipath-based SLAM: Combining information from multiple propagation paths,” *IEEE Trans. Signal Process.*, vol. 71, pp. 4011–4028, Sep. 2023.
- [17] X. Li, B. Deutschmann, E. Leitinger, and F. Meyer, “Adaptive multipath-based SLAM for distributed MIMO systems,” 2025, arXiv. [Online]. Available: <https://arxiv.org/abs/2506.21798>
- [18] F. Kschischang, B. Frey, and H.-A. Loeliger, “Factor graphs and the sum-product algorithm,” *IEEE Trans. Inf. Theory*, vol. 47, no. 2, pp. 498–519, Feb. 2001.
- [19] H.-A. Loeliger, “An introduction to factor graphs,” *IEEE Signal Process. Mag.*, vol. 21, no. 1, pp. 28–41, Feb. 2004.
- [20] V. Savic and E. G. Larsson, “Fingerprinting-based positioning in distributed massive MIMO systems,” in *Proc. IEEE VTC 2015*, Sept. 2015, pp. 1–5.
- [21] A. Fascista, B. J. B. Deutschmann, M. F. Keskin, T. Wilding, A. Coluccia, K. Witrals, E. Leitinger, G. Seco-Granados, and H. Wymeersch, “Uplink joint positioning and synchronization in cell-free deployments with Radio Stripes,” in *Proc. IEEE ICC 2023*, Rome, Italy, May 2023.
- [22] —, “Joint localization, synchronization and mapping via phase-coherent distributed arrays,” *IEEE J. Sel. Top. Signal Process.*, vol. 19, no. 2, pp. 412–429, Mar. 2025.
- [23] V. Tentu, H. Wymeersch, M. F. Keskin, S. Dey, and T. Svensson, “Phase-coherent D-MIMO ISAC: Multi-target estimation and spectral efficiency trade-offs,” in *Proc. IEEE JC&S 2026*, Feb. 2026.
- [24] A. Richter, “Estimation of radio channel parameters: models and algorithms,” Ph.D. dissertation, Ilmenau University of Technology, 2005.
- [25] T. L. Hansen, B. H. Fleury, and B. D. Rao, “Superfast line spectral estimation,” *IEEE Trans. Signal Process.*, vol. PP, no. 99, 2018.
- [26] S. Grebien, E. Leitinger, K. Witrals, and B. H. Fleury, “Super-resolution estimation of UWB channels including the dense component—an SBL-inspired approach,” *IEEE Trans. Wirel. Commun.*, pp. 10301 – 10318, Feb. 2024.
- [27] F. Meyer, T. Kropfreiter, J. L. Williams, R. Lau, F. Hlawatsch, P. Braca, and M. Z. Win, “Message passing algorithms for scalable multitarget tracking,” *Proc. IEEE*, vol. 106, no. 2, pp. 221–259, Feb. 2018.
- [28] Y. Bar-Shalom, P. K. Willett, and X. Tian, *Tracking and Data Fusion: a Handbook of Algorithms*. Storrs, CT, USA: Yaakov Bar-Shalom, 2011.
- [29] T. Wilding, S. Grebien, E. Leitinger, U. Mühlmann, and K. Witrals, “Single-anchor, multipath-assisted indoor positioning with aliased antenna arrays,” in *Asilomar-18*, Pacific Grove, CA, USA, Oct. 2018, pp. 525–531.
- [30] E. Leitinger, S. Grebien, and K. Witrals, “Multipath-based SLAM exploiting AoA and amplitude information,” in *Proc. IEEE ICCW-19*, Shanghai, China, May 2019.
- [31] X. Li, E. Leitinger, A. Venus, and F. Tufvesson, “Sequential detection and estimation of multipath channel parameters using belief propagation,” *IEEE Trans. Wirel. Commun.*, vol. 21, no. 10, pp. 8385–8402, Apr. 2022.
- [32] Taichi Lang, <https://github.com/taichi-dev/taichi>, gitHub repository.